Dalton Transactions

An international journal of inorganic chemistry

Accepted Manuscript

ROYAL SOCIETY OF CHEMISTRY

rsc.li/dalton

View Article Online
DOI: 10.1039/D4DT03498H

ARTICLE

Unveiling surface reactivity: the crucial role of auxiliary ligands in Gallium amidinate-based precursors for Atomic Layer Deposition

Received 00th January 20xx,
Accepted 00th January 20xx

DOI: 10.1039/x0xx00000x

Eva Pugliese,[a,b] Damien Coutancier,[a] Paul-Alexis Pavard,[a] Julien Hervochon,[a] Bram van der Linden,[c,d] Nicolas Casaretto,[b] Sophie Bourcier,[b] Geoffrey Pourtois,[d] Muriel Bouttemy,[a,e] Audrey Auffrant,[b] and Nathanaelle Schneider[a,*]

Two novel gallium precursors for Atomic Layer Deposition (ALD), **$LGaMe_2$** and **$LGa(NMe_2)_2$** with L = N,N'-di-*tert*butylacetamidinato, were successfully synthesised from a carbodiimide and gallium trichloride. The compounds were characterised by NMR spectroscopy and HR-mass spectrometry, confirming their monomeric nature. Their surface reactivity under ALD conditions with H_2O and H_2S co-reactants was explored using in-situ quartz crystal microbalance (QCM) measurements. **$LGaMe_2$**, bearing methyl ligands, was found to inhibit film growth, with deposition halting after three cycles. In contrast, **$LGa(NMe_2)_2$** facilitated the successful growth of films using both H_2O and H_2S leading to Ga_2O_3 and Ga_2S_3 respectively, as confirmed by additional thin film ex-situ characterisation.This study underscores the critical role of auxiliary X ligands (here Me or NMe_2) in determining ALD process efficiency, and emphasises the complexity and unique nature of surface chemistry compared to solution-phase behaviour.

Introduction

In homogeneous organometallic catalysis, functionalised hybrid ligands are of utmost importance to tune the electronic and steric properties of the metal.[1–4] Generally, the reaction employs a precatalyst of the type [LMX] where L is a functionalised ligand, M the metal centre, and X an auxiliary ligand. In the reaction conditions this precatalyst is transformed into the active species, through the modification of the X ligand, often a halide, which can be substituted by an hydride,[5,6] or a carbon-based group[7–12], with in some cases a change in the oxidation state of the metal. The catalytic process can also be initiated by the migration of the X group, as in polymerization involving a coordination-insertion mechanism where X is generally alkoxide or an amide.[13–15] But in all those cases, the functionalised multidentate ligand remains intact and it is essential for the catalysis as its strong interaction with the metal participates to ensure optimal catalytic properties and in some cases stereoselectivity.[1,16–19] However, the fate of the functionalised ligand may not be similar in surface chemistry. In the field of surface organometallic chemistry, heteroleptic complexes of the LMX type generally react with a silica surface by release of the X anionic ligand.[20] In Atomic Layer Deposition (ALD), organometallic compounds are used as metal atom sources. The ligand design has the essential function of tuning the volatility, stability and surface reactivity of the metal complex. The use of heteroleptic complexes has gained growing interest in recent works, thanks to the dissymmetry they induce, often associated to a better volatility and reactivity.[21] Amidinate ligands are already present in different commercial ALD precursors and are subject of numerous studies on the development of novel precursors.[22–25] Most commonly, they are used in homoleptic complexes, mainly with different first or second row transition metals (Co, Ni, Fe, Zr, Cu, Mn, Mo, Sn, Ca, …), [26–35] but also in combination with cyclopentadienyl ligands in the case of the large lanthanide ions (La, Ce, Gd, Dy, Er, …).[36–39] The surface reactivity of heteroleptic complexes has been investigated either by computational models[23,40] or also in combination with *operando* mass spectrometry.[38] The ligand lability of complexes bearing an amidinate and alkyl ligands has also been studied using *ex-situ* solid-state NMR (SS-NMR), with findings in agreement with homogeneous catalysis principles.[41]

Gallium oxide (Ga_2O_3) is a wide-bandgap semiconductor with significant potential in applications such as power electronics, UV photodetectors, and transparent conductive oxides, attributed to its high breakdown voltage, excellent thermal stability, and electrical properties.[42–44] Gallium sulphide (Ga_2S_3), another promising wide-bandgap material, has attracted attention for optoelectronic and catalytic applications, particularly in light-driven processes, due to its tunable bandgap and favourable electronic characteristics.[45–47] Both Ga_2O_3 and Ga_2S_3 are polymorphic and have been synthesised using various techniques, but the growth of

[a] Institut Photovoltaïque d'Île-de-France (IPVF), UMR 9006, CNRS, Ecole Polytechnique - IP Paris, Chimie Paristech - PSL, 18 Boulevard Thomas Gobert, Palaiseau, 91120, France
[b] Laboratoire de Chimie Moléculaire (LCM), CNRS, École Polytechnique, Institut Polytechnique de Paris, Route de Saclay, 91120 Palaiseau, France.
[c] Department of Chemistry, KU Leuven, Celestijnenlaan 200F, 3001 Leuven, Belgium
[d] IMEC, Kapeldreef 75, 3001 Leuven, Belgium
[e] Institut Lavoisier de Versailles (ILV), Université de Versailles Saint-Quentin-en-Yvelines, Université Paris-Saclay, CNRS, UMR 8180, 78035Versailles CEDEX, France
† Email: nathanaelle.schneider@cnrs.fr.
Supplementary Information available: See DOI: 10.1039/x0xx00000x

stoichiometric species with controlled phase remains a significant challenge.

ALD is particularly advantageous in this context, as it enables precise control over composition, phase, and thickness. Recent efforts to fabricate Ga containing films using ALD, mostly Ga_2O_3, GaN, GaP and Ga_xS, have relied on a limited number of gallium precursors, namely trimethyl[48–62] and triethylgallium,[50,63–79] gallium chloride,[80–83] tris(dimethylamido) gallium (TDMAG),[84–90] and gallium acetylacetonate,[91] highlighting the need for new, optimised precursor molecules. As pointed out earlier, amidinate ligands, known for their thermal stability and tunability, have shown promise as components in precursor design.

In this study, we explore the ALD chemistry of gallium amidinate complexes to address the challenges associated with the growth of Ga_2O_3 and Ga_2S_3 thin films. We developed two novel amidinate gallium complexes as precursors for the ALD of GaS_x and GaO_x materials. Their reactivity, which could not be expected from assumptions based on solution chemistry, prompted us to perform a mechanistic study based on mass evolutions followed by Quartz Crystal Microbalance (QCM), thin films characterization and modelling by Density Functional Theory (DFT).

Results

Synthesis of the Ga-based metal-organic compounds

Dagorne *et al.* have described the synthesis of a series of sterically crowded amidinate gallium dichloride and dimethyl complexes by reaction of the gallium chloride with the preformed amidinate reagent, followed by reaction with Grignard reagent.[92] To achieve a volatile and thermally stable complex, we employed a small nucleophile (CH_3^-) and a symmetric carbodiimide without α-hydrogens on the nitrogen atoms, while ensuring sufficient steric hindrance to protect the metal center; therefore, N,N'-Di-tert-butylcarbodiimide was selected. Inspired by this, we synthesised **$LGaCl_2$** with L= N,N'-di-*tert*butylacetamidinato in two steps from di-*tert*butylcarbodiimide with a 41 % yield over two steps (Scheme 1).

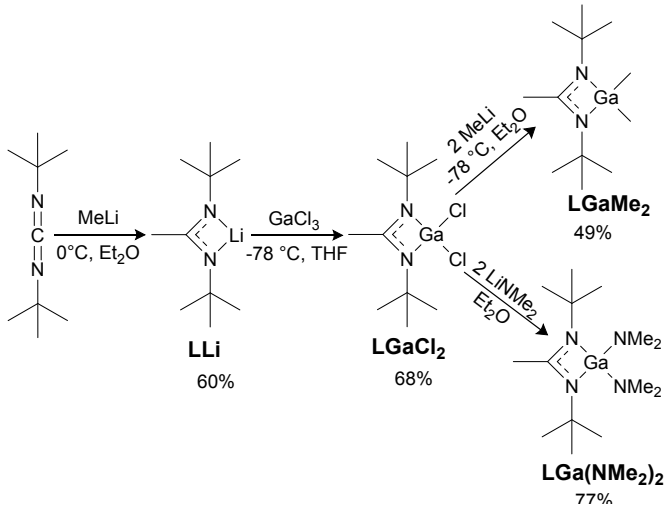

Scheme 1 - Synthesis of **$LGaMe_2$** and **$LGa(NMe_2)_2$** complexes (L=*t*BuNCMeNtBu).

To increase the volatility of the complex and avoid the use of halide substituents, we then substituted chlorides by methyl and dimethylamide groups using MeLi and $LiNMe_2$ respectively (see Experimental for further details). For each step, the products were characterised by ^{1}H-NMR, ^{13}C-NMR and HRMS (see Experimental Section and SI). Single crystals were obtained for **$LGaCl_2$** (see Figure 1, Table S1) and **LLi** (Figure S9), while **$LGaMe_2$** and **$LGa(NMe_2)_2$** obtained as oily products could not be crystallised despite several attempts. **$LGaCl_2$** crystallises as a monomer where the gallium adopts a tetrahedral geometry (see Figure 1). Compared to the $\{^tBuC(NtBu)_2\}GaCl_2$ complex described by Dagorne *et al.*,[92] the **$LGaCl_2$** complex presents a larger N1-C9-N2 angle and smaller C1-N1-C9 and C5-N2-C9 angles due to the reduced steric hindrance of the methyl group compared to the *tert*-butyl amidinate described in the literature. The bond lengths within the ligand (N1-C1 and N2-C9) are shorter, while the Ga1-N coordination bond is slightly longer in our case than what was reported for the $\{^tBuC(N^tBu)_2\}GaCl_2$ complex. The substitution of chlorides by methyl and dimethylamido groups was confirmed by ^{1}H-NMR spectroscopy and HR-mass spectrometry. NMR data also allow ascertaining the monomeric nature of both **$LGaMe_2$** and **$LGa(NMe_2)_2$** (Figures S1-S8).

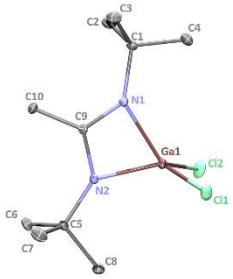

Figure 1 - X-ray structure of **$LGaCl_2$** (with thermal ellipsoids drawn at the 20% probability level). The H atoms are omitted for clarity. Selected bond lengths [Å] and angles [°]: Ga1-N1= 1.943(2); Ga1-Cl1= 2.1546(7); N1-C1 = 1.476(3); N1-C9 = 1.331(3); N1–C9–N2 = 109.5(2); C1–N1-C9 = 131.6(2); C5-N2-C9 = 131.0(2).

Atomic Layer Deposition (ALD) of Ga-based inorganic thin films

The two gallium complexes **$LGaMe_2$** and **$LGa(NMe_2)_2$** were used as gallium precursors in ALD reactor for the deposition of GaO_x and GaS_x by using H_2O and H_2S co-reactants respectively. To understand their impact on film growth, surface reactivity was elucidated by in-situ quartz crystal microbalance (QCM) measurements, which recorded mass variations occurring during each pulse/purge times of the deposition process. The deposition temperature was set at 150 °C, and the Ga precursor source was kept at 50 °C. Figure 2 shows the mass variations measured during the deposition process combining **$LGaMe_2$** and **$LGa(NMe_2)_2$** with H_2O (Figure 2a) and H_2S (Figure 2b) over 15 cycles. The QCM curves obtained with the **$LGaMe_2$** precursor indicate that material growth ceases after the first two or three cycles, regardless of whether H_2O or H_2S is used as co-reactants. In contrast, under the same conditions with the **$LGa(NMe_2)_2$**

View Article Online
DOI: 10.1039/D4DT05408H

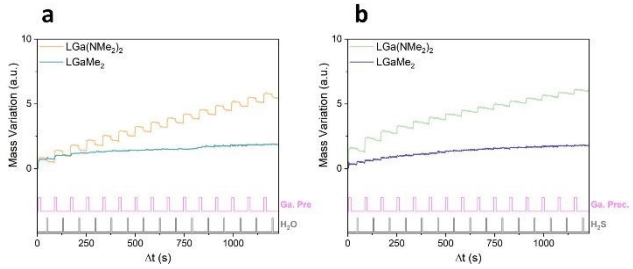

Figure 2 - Mass variations measured by in situ QCM measurements during ALD of GaOx (a) and GaS_x (b) at T_{dep} = 150°C from the gallium precursors **$LGaMe_2$** and **$LGa(NMe_2)_2$** . The lower part of the graphs indicates the pulse sequence.

precursor, the QCM curves exhibit linear growth over time after the initial five cycles, which is characteristic of an ALD process. To better visualise this striking difference, 15 cycles are overlaid (Figures 3, S11, S12). For reference and to validate the methodology, similar experiments were conducted using the commercial gallium precursor tris(dimethylamido)gallium (**TDMAG**) and the resulting QCM profiles were compared (Figure S10, S13, S14).

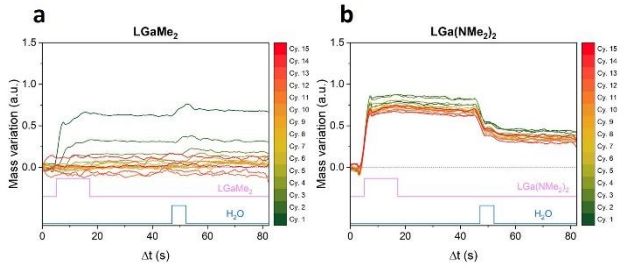

Figure 3 - Overlay of 15 consecutive cycles of ALD of GaO_x measured by *in situ* QCM using **$LGaMe_2$** (**a**) and **$LGa(NMe_2)_2$** (**b**) as gallium precursors. Green traces indicate initial cycles and red traces the last ones (15 total cycles).

Properties of Ga-based inorganic thin films

To further characterise the precursors and materials produced via the ALD process, GaO_x and GaS_x films were deposited on Si substrates with native oxide, producing sufficiently thick films to analyse their morphology and composition. The number of cycles were set according to mass variations determined by QCM measurements to ensure the deposition of films with comparable thicknesses. Hence, GaO_x films were obtained with 150 cycles or 400 cycles using **TDMAG** or **$LGa(NMe_2)_2$** as gallium source respectively. The films were characterised by ellipsometry, which gave 13.6 nm and 22.9 nm film thicknesses (Figures S17, S18), corresponding to growth per cycle (GPC) values of 0.91 Å/cycle and 0.56 Å/cycle for **TDMAG** and **$LGa(NMe_2)_2$** respectively. Same number of cycles were applied for the deposition of GaS_x films, which yielded 19.7 nm film using commercial **TDMAG** precursor, and 5.1 nm film with **$LGa(NMe_2)_2$** precursor (Figures S19, S20), corresponding to GPC values of 1.31 Å/cycle and 0.13 Å/cycle. Film thicknesses were also evaluated by XRR, finding comparable values (Figures S21-S24).

The composition and chemical fine structure of the thin films were determined by XPS (X-ray Photoelectron Spectroscopy, see corresponding survey spectra in Figure S25). Except Silicon detection in the case of the ultrathin GaS_x film deposited with **$LGa(NMe_2)_2$**, only the constitutive elements and adventitious carbon appear on the spectra. Notably, the XPS probed depth is approximately 10 nm, ensuring that for the other samples the acquired data represent more than half of the layer. High-energy resolution spectra were collected at the surface of the deposited films, without sputtering to eliminate the surface contamination, to avoid preferential sputtering artefacts. Figure 4 and Figures S26 and S27 show the high energy resolution XPS spectra of the main elements - Ga 2p, S 2p, O 1s, N 1s, and C 1s - across all films. For quantification, the Ga 2p peak was preferred to Ga 3s, which partly overlaps with O 2s at high binding energy. As shown in Figure 4a and Figure S26a, all the Ga-containing films exhibit the characteristic doublet peaks of Ga 2p with energy position of the main Ga $2p_{3/2}$ peak at 1118.4 eV and 1118.3 eV when **$LGa(NMe_2)_2$**/H_2O or **$LGa(NMe_2)_2$**/H_2S was used. No metallic Ga contribution is detected at 1116.5 eV[93] neither from Ga 3d region examination (contribution at 18.7 eV[94]). Ga 2p energy position is then associated to the oxidation states of Ga^{III} in both cases, consistent with literature values.[95] To identify other potential Ga-containing phases, the Ga 3d transition spectral region was explored in the low binding energy region, and contribution of Ga-N bonding (expected at 19.74 eV[94]) can be excluded. When H_2S is used, the S 2p core level spectra overlaps with Ga 3s but can be deconvoluted, leading to S $2p_{3/2}$ positions at 163.2 eV (**TDMAG**) and 162.9 eV (**$LGa(NMe_2)_2$**). No evidence of sulfates or sulfites, whose signals typically appear in the S 2p region around 169-170 eV (not shown), was detected in the films.[94] A high O 1s signal is observed for Ga-O films with a main contribution at 531.2 eV assigned to oxygen-metal bonds, consistent with gallium oxide references[96] to the oxide environment. A second contribution at higher binding energy is measured for all films and attributed to the adventitious surface contamination as confirmed by C 1s peak deconvolution (Figure S27). The N 1s spectral region is superimposed with Ga Auger signals Ga L_2 $M_{4,5}M_{4,5}$ preventing N detection as it is also supposed to only concern residues of precursor. Interestingly, C-N and C=N bonds are necessary to fit the C 1s peak, in addition to conventional C-C and C-O, C=O and COOH bonds inherent to carbonaceous surface contamination (Figure S27). The carbon content was measured as 10 to 15 at. % of the total elements for the oxides grown with **TDMAG** and **$LGa(NMe_2)_2$** precursors, respectively. In the sulphides, higher carbon contamination around 25 at. % was observed (Table S2). Finally, the XPS analysis revealed an average atomic composition of 36.4 % Ga, 49.9 % O and 44.6 % oxide, 13.2 % C and <1 % N when H_2O was used, and 28.2 % Ga, 30.5 % S, 10.6 % O, 27 % C and ≈ 4 % N when H_2S was used (more details can be found in Table S2). These values correspond to the Ga/Y ratios (Y=O, S) of 0.88 and 0.75 for GaO_x obtained from **TDMAG**

View Article Online DOI: 10.1039/D4DT03408H

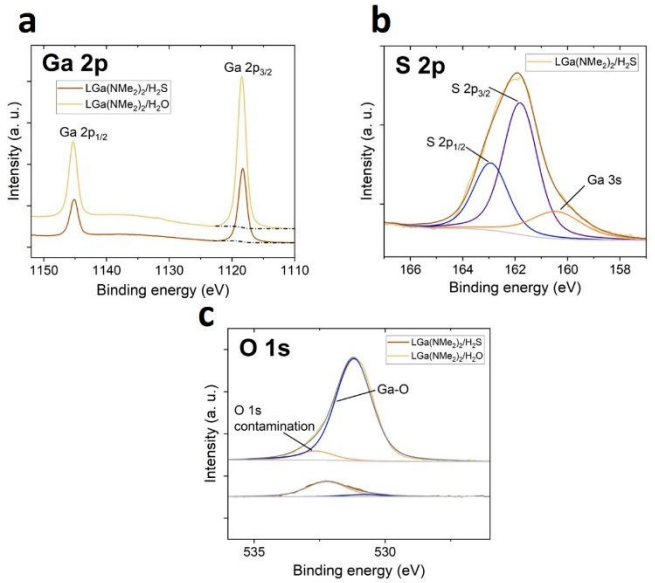

Figure 4 - High energy resolution spectral regions of the main elements of Ga-containing films obtained from **LGa(NMe$_2$)$_2$** precursor (a) Ga 2p (b) S 2p/Ga3s (c) O 1s.

and **LGa(NMe$_2$)$_2$** respectively; and of 0.87 and 1.0 for the GaS_x films deposited with **TDMAG** and **LGa(NMe$_2$)$_2$** respectively. The theoretical Ga/Y ratio for a Ga_2Y_3 stoichiometry is 0.67, which supports the presence of Ga^{III} species in both the oxide and sulphide materials. Variations from the theoretical value can be attributed to the additional oxygen content in Ga-S films.

Discussion

Ga_2O_3 and Ga_2S_3 thin films were successfully prepared via ALD using the novel Ga-amidinate based precursor, **LGa(NMe$_2$)$_2$**, in combination with H_2O or H_2S on Si wafer substrates. XPS analysis confirmed the Ga_2Y_3 stoichiometries of the resulting films. However, when the amido ligand is replaced with a methyl group, as in the case of **LGaMe$_2$**, ALD growth stops after just 3 cycles. This striking difference in surface reactivity between the two gallium amidinate precursors prompted further investigation into the film growth mechanism.

Due to their heteroleptic nature, the **LGaMe$_2$** and **LGa(NMe$_2$)$_2$** complexes can react with the surface sites following two possible ways, described as two simplified models (see Scheme 2). Either the auxiliary ligands X can be released (model A, Scheme 2), or the chelating L ligand will be exchanged to form bonds with the surface (model B, Scheme 2). Previous studies in solution chemistry of gallium complexes of the $LGaX_2$-type (with L indicating a generic bidentate ligand and X an alkyl or alkylamido ligand) report that model A is expected to be more favourable, in reacting both with oxygen[97–99] or sulphur sources.[100] To investigate our specific case, we first used Density Functional Theory (DFT) to calculate the enthalpies of the two reactions of the proposed models for both precursors. To speed up the calculations, the surface reactions were simplified as gas-phase reactions at 0 K between the precursor molecule and a $Si(OH)_4$ molecule that simulates the Si wafer substrate. Details of the reactions considered can be found in the SI (Figure S28 and Table S3). The reactions that correspond to model A (detachment of the X ligands) yielded enthalpy values of -0.68 eV for **LGaMe$_2$** and of -0.14 eV for **LGa(NMe$_2$)$_2$**. On the other hand, model B (detachment of the amidinate ligand), yielded enthalpies of 0.23 eV for **LGaMe$_2$** and 0.17 eV for **LGa(NMe$_2$)$_2$**, which indicates less favourable thermodynamics, in agreement with the reported solution studies. Calculations with larger Si-based clusters to mimic the SiO_2 surface such as $(HO)_3Si\text{-}O\text{-}Si(OH)_3$ and $(HO)Si(OSiH_3)_3$,[101] with incorporation of a DFT-D3 Grimme dispersion correction,[102] led to the same trends. Model A is thermodynamically favoured over model B and results in a much larger energy release for $LGaMe_2$, whereas model B results in similar reaction energies for both precursors. For example, model A leads to enthalpy values of -1.55 eV for **LGaMe$_2$** and -0.82 eV for **LGa(NMe$_2$)$_2$** with $(HO)_3Si\text{-}O\text{-}Si(OH)_3$, while model B yields 0.25 eV for **LGaMe$_2$** and 0.26 eV for **LGa(NMe$_2$)$_2$** with $(HO)Si(OSiH_3)_3$. Because in the calculations we are only looking at the very first adsorption step on the Si_{ox}/Si surface, with a simplified model and without considering kinetics, the results of DFT do not match what we observed experimentally in QCM.

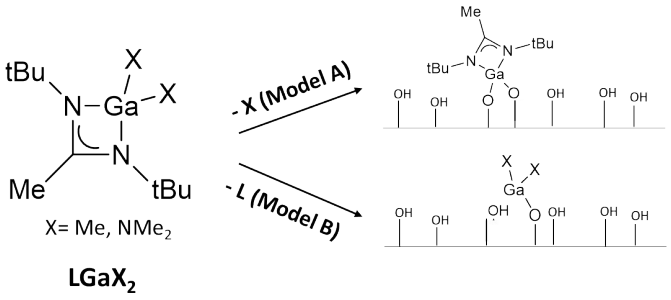

Scheme 2 - Interaction of the **LGaMe$_2$** and **LGa(NMe$_2$)$_2$** complexes with the substrate surface sites upon metal precursor pulse.

In fact, in the case of model A, we would expect the two precursors to have comparable film growth. Additional investigations are thus necessary to explain the experimental observations.

Experimentally, it is possible to analyse the QCM profiles of mass gain and loss during each pulse, to gain information about the fragments released – and consequently, the relative lability of the ligands. To achieve this, we adapted the model proposed by Meng *et al.* [84] for the growth or Ga_2S_3 from TDMAG and H_2S, and extended it to the case of TDMAG/H_2O (see Figure S16 and eq. S3, S4). A detailed description of the simpler case involving the homoleptic complex **TDMAG** is provided in the SI.

When considering the heteroleptic complexes **LGaMe$_2$** and **LGa(NMe$_2$)$_2$**, we can write out the equations that describe the surface reactions of the generic complex **LGaX$_2$** (with X=Me or NMe_2) with H_2Y (with Y=O or S) for each simplified model, as follows.

Model A – release of X type ligand upon metal precursor pulse

$$\vdash (YH)_n + LGaX_2 \rightarrow \vdash Y_nGaLX_{(2-n)} + n\,HX$$

$$\vdash Y_nGaLX_{(2-n)} + 1.5\,H_2Y \rightarrow \vdash Y_{1.5}Ga(YH)_n + HL + (2-n)\,HX$$

Where " ⊢ " represents the surface, "*n*" the number of surface sites reacting and all the reactants not bound to the surface are in the gaseous phase.

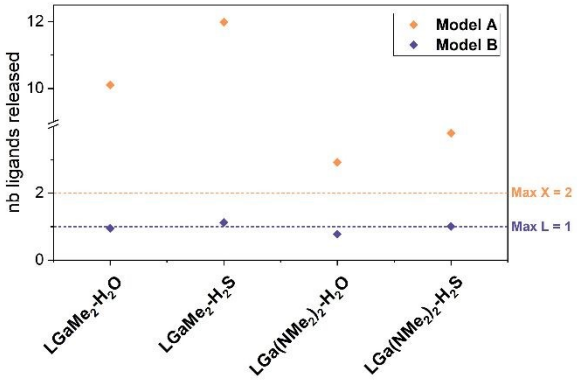

Figure 5 - Fitting of the experimental measured by QCM mass variations, averaged over 10 cycles. Orange dots: data fitting following model A; blue dots: data fitting following model B. Dotted lines: maximum theoretical values in the two models due to the stoichiometry of the complexes.

From here we can extract the expressions for Δm (mass variation after one cycle) and m_1 (mass variation after the pulse of metal precursor), being:

$$\Delta m = \mathrm{Y}_{1.5}\mathrm{Ga(YH)}_n - (\mathrm{YH})_n = \mathrm{GaY}_{1.5}$$
$$m_1 = \mathrm{Y}_n\mathrm{GaLX}_{(2-n)} - (\mathrm{YH})_n = \mathrm{Ga} + 2\mathrm{X} + \mathrm{L} - n\ \mathrm{HX}.$$

On the other hand, if L ligand is the one reacting with the surface we will have:

Model B– release of L ligand upon metal precursor pulse

$$\vdash (\mathrm{YH})_n + \mathrm{LGaX}_2 \rightarrow \vdash \mathrm{Y}_n\mathrm{GaX}_2(\mathrm{L})_{(1-n)} + n\ \mathrm{HL}$$
$$\vdash \mathrm{Y}_n\mathrm{GaX}_2\mathrm{L}_{(1-n)} + 1.5\ \mathrm{H_2Y} \rightarrow \vdash \mathrm{Y}_{1.5}\mathrm{Ga(YH)}_n + (1-n)\mathrm{HL} + 2\ \mathrm{HX}$$

With the corresponding equations:

$$\Delta m = \mathrm{Y}_{1.5}\mathrm{Ga(YH)}_n - (\mathrm{YH})_n = \mathrm{GaY}_{1.5}$$
$$m_1 = \mathrm{Y}_n\mathrm{GaX}_2\mathrm{L}_{(1-n)} - (\mathrm{YH})_n = \mathrm{Ga} + 2\ \mathrm{X} + \mathrm{L} - n\ \mathrm{HL}$$

By combining the mass variation equations with the experimental ratio calculated for $\Delta m/m_1$, we can extract "*n*" as an index of the number of sites reacting with the same metal precursor.

By fitting the experimental data with the two proposed models, it was determined that, for both **LGaMe$_2$** and **LGa(NMe$_2$)$_2$** complexes, the L chelating ligand is the first to dissociate during the surface reaction (model B; see Figure 5 and Scheme 2). In Figure 5, we can observe a good match between the experimental data fitted with model B (blue dots) and the maximum theoretical value of number of ligands detaching (one for the L ligand given its 1:1 stoichiometry with the Ga metal centre, and two for the X ligands; see dotted lines).This unexpected finding highlights how the reactivity in solution and on surfaces can be very different, and explains the different film growth behaviour observed in our study and by others.[48,57–62,86,103,104] For **LGaMe$_2$**, the dissociation leaves ⊢YGaMe$_2$ moieties on the surface, which do not react with H_2Y co-reactants. This behaviour can be compared to that of the commercial trimethyl gallium precursor, which requires more reacting co-reactants than H_2O to grow a film of Ga_2O_3 (ozone[59–61], O_2 plasma[48,57,58,61,62,103,104]). This very low reactivity can be attributed to the very stable Ga-Me surface groups. Indeed high activation barriers were calculated to remove the methyl group through water Ea(Ga-CH_3) = 151.0 kJ/mol.[105] Similarly, TMG is not reactive with H_2S for the growth of Ga_2S_3 films.[86] In contrast, the **LGa(NMe$_2$)$_2$** complex dissociates to leave ⊢YGa(NMe$_2$)$_2$ moieties on the surface, a scenario analogous to the well-known **TDMAG** precursor. This makes **LGa(NMe$_2$)$_2$** well-suited for the growth of Ga_2O_3 and Ga_2S_3 films, as highlighted in the results section. When comparing the **TDMAG** precursor and **LGa(NMe$_2$)$_2$**, the faster growth rate observed for **TDMAG** can be attributed to the smaller steric hindrance of the NMe_2 ligand compared to L chelating ligand, allowing for greater surface sites coverage.

Conclusions

Two novel gallium precursors for ALD, **LGaMe$_2$** and **LGa(NMe$_2$)$_2$**, featuring amidinate ligands, were successfully synthesised and characterised. Their surface reactivity was investigated using in-situ quartz crystal microbalance (QCM) measurements. It was found that **LGaMe$_2$**, which bears methyl ligands, does not allow film growth with either H_2O or H_2S co-reactants, as growth halts after only three cycles. In contrast, **LGa(NMe$_2$)$_2$** enables the successful formation of ALD films with both H_2O and H_2S.

This contrasting behaviour highlights the crucial role played by the auxiliary X ligands (here Me or NMe_2) in the ALD process, which appears to have a greater influence on the film growth than the chelating amidinate. These findings, in contrast with classic coordination chemistry dogma, highlight the complexity of surface chemistry and its distinct nature compared to solution chemistry.

By combining QCM analysis, film characterisation and DFT, this work provided valuable insights into the surface reaction mechanisms, offering a foundation for the design and developments of future molecular precursors optimised for ALD applications.

Experimental

Molecular Synthesis

LLi: MeLi (8.1 mL; 13.0 mmol; 1.0 equiv.) was added dropwise to a solution of ditert-butyl carbodiimide (2.5 mL; 13.0 mmol; 1.0 equiv.) in diethyl ether (20 mL) at 0 °C. After 30 min of stirring at room temperature, the solvent was evaporated. The product was isolated as a white solid and washed with pentane (1.38 g; 60%). ^{1}H-NMR (THF-d_8): δ 1.94 ppm (s, 3H, CMe_2); 1.11 ppm (s, 18H, CMe_3). ^{13}C-NMR (THF-d_8): δ 169.0 ppm (s, N*C*N); 50.4 ppm (s, N*C*Me$_3$); 34.2 ppm (s, *C*Me$_3$); 19.2 ppm (s, *C*Me).

LGaCl$_2$: **LLi:** (800.4 mg; 4.5 mmol; 1.0 equiv.) was dissolved in THF (20 mL) and placed at -78 °C. The gallium trichloride salt (815.4 mg in 20 mL of THF; 4.6 mmol; 1.0 equiv.) was added with a canula to the ligand solution and the crude was left stirring overnight upon warming back to room temperature. The solvent was evaporated under vacuum and the solid was purified by sublimation at 85 °C and 5*10^{-2} mbar, yielding a white solid (0.96 g; 68%). ^{1}H-NMR (THF-d_8): δ 2.38 ppm (s, 3H, CMe); 1.34 ppm (s, 18H, N^{t}Bu). ^{13}C-NMR (THF-d_8): δ 176.0 ppm (s, N*C*MeN); 53.2 ppm (s, N*C*Me$_3$); 31.4 ppm (s, *C*Me$_3$); 17.0 ppm

(s; *C*Me). HR-MS Pos (APCI): $[LGaCl]^+$ calcd. *m/z* 273.0644 for $C_{10}H_{21}ClGaN_2^+$; found *m/z* 273.0655.

$LGaMe_2$: MeLi (1.6 mL; 1.6 mmol; 2.2 equiv.) was added dropwise at -78 °C to a solution of **$LGaCl_2$** (230.6 mg; 0.7 mmol; 1.0 equiv.) in diethyl ether (10 mL). The crude was then stirred at room temperature overnight. The solvent was then evaporated by vacuum at -40 °C and the final complex was purified by distillation, yielding a transparent oil (98.0 mg; 49%). ^{1}H-NMR (THF-d_8): δ 2.12 ppm (s, 3H, CMe); 1.19 ppm (s, 18H, N^{t}Bu); -0.34 ppm (s, 6H, $GaMe_2$). ^{13}C-NMR (THF-d_8): δ 169.6 ppm (s, N*C*MeN); 51.4 ppm (s, N*C*Me_3); 31.9 ppm (s, *C*Me_3); 17.9 ppm (s, *C*Me); -6.0 ppm (s, $GaMe_2$). HR-MS Pos (APCI): $[LGaMe_2]^+$ calcd. *m/z* 269.1503 for $C_{12}H_{28}GaN_2H^+$; found *m/z* 269.1510.

$LGa(NMe_2)_2$: $LiNMe_2$ (472 mg; 9.25 mmol; 2 equiv.) was added at room temperature to a solution of **$LGaCl_2$** (1.42 g; 4.60 mmol; 1 equiv.) in Et_2O, 20 mL. The reaction mixture was stirred overnight. The solvent was removed by evaporation under vacuum. **$LGa(NMe_2)_2$** was then obtained after distillation as a colourless oil (3.53 mmol; 77 %). ^{1}H-NMR (THF-d_8): δ 2.70 (s, 12H, $GaNMe_2$), 2.22 (s, 3H, CMe), 1.34 (s, 18H, N^{t}Bu). ^{13}C-NMR (THF-d_8): δ 171.9 ppm (s, N*C*MeN); 50.8 ppm (s, N*C*Me_3); 42.5 ppm (s, NMe_2); 31.4 ppm (s, *C*Me_3); 16.7 ppm (s, *C*Me). HR-MS Pos (APCI): $[LGa(NMe_2)_2H]^+$ calcd. *m/z* 327.2034 for $C_{14}H_{34}GaN_4^+$; found *m/z* 327.2033.

Thin film fabrication by ALD

Thin films were prepared in a BENEQ TFS-200 ALD reactor. **TDMAG** ($[Ga(NMe_2)_3]_2$, 98%, Strem Chemicals), **$LGa(NMe_2)_2$**, **$LGaMe_2$**, H_2S (99.5%, Air Liquide), and deionised water were used as gallium, sulphur and oxygen sources respectively. Nitrogen (N_2, 99.9999%, Air Liquide) was used as both carrier and purging gas. Ga sources were heated in a hot solid source system Beneq HS300 at 50°C (**$LGa(NMe_2)_2$**, **$LGaMe_2$**) or 70°C (**TDMAG**), while other precursors were kept at room temperature. Experiments were performed at T_{dep} = 150°C, and the pressure in the reaction chamber was kept in the range of 1−2 mbar. Thin films were deposited on single polished n-doped Si (100) wafer with a native oxide top layer. Prior to deposition, substrates were cleaned in a detergent solution (RBS 35 Concentrate, 2% in water, 5 min) and rinsed with deionised water.

A gallium oxide (or sulphide) growth cycle, i.e., $\{GaO_x\}$ or $\{GaS_x\}$, corresponds to $\{GaO_x\}$ (or $\{GaS_x\}$) = $\{[Ga]/N_2/H_2O$ (or $H_2S)$ $/N_2$ = [0.8/0.03/0.3/1.6]/5/0.8/5 s}, and "combination" mode was chosen to ensure proper mass transport of Ga source. "Combination" mode is composed of four steps ($[t_1/t_2/t_3/t_4]$). First, N_2 is injected in the Ga source (t_1), then all valves are kept closed (t_2), and the Ga precursor is pulsed (t_3). Finally, N_2 is injected with a simultaneous precursor pulse (t_4). For the final films, the ALD sequence was repeated for 150 cycles in the case of **TDMAG** precursor, and for 400 cycles for the **$LGa(NMe_2)_2$** precursor.

Thin film characterization

Film characterizations were carried out on the as-deposited thin films. Thickness was determined by spectroscopic ellipsometry (SE) using a Horiba Jobin Yvon Uvisel 2 ellipsometer. The SE measurement was performed at incidence angle of 70◦ in energy range between 1.5 and 5.0 eV with step of 0.05 eV, and the data were fitted using DeltaPsi2 software modelled with TaucLorentz oscillators functions with parameters adapted from Fujiwara and Collins. [106] X-ray reflectivity (XRR) measurement, using PANalytical Empyrean equipment with Cu Kα radiation source (λ = 0.15418 nm) operated at 45 kV and 40 mA, was performed for further determination of the thickness, the roughness, and the density of fabricated thin films. The surface and in-depth chemical compositions were analysed using x-ray photoelectron spectroscopy (XPS) with Thermo Electron™ NEXSA spectrometer equipped with a monochromatic Al-Kα x-ray source (hv = 1486.6 eV). The spectrometer was calibrated using Cu and Au samples following the ASTM-E-902-94 protocol. A X-ray beam diameter of 400 µm was used for both surface points and depth profiles. The flood gun was not necessary. The survey scans (0–1350 eV) were collected at a pass energy of 200 eV, 100 ms dwell time, and a step size of 1 eV. High-energy resolution spectra were measured at a pass energy of 20 eV, 100 ms dwell time, with a step size of 0.1 eV. An energy calibration was realised with respect to the C 1*s* peak at 284.8 eV. Avantage Software was employed for quantification and atomic composition determination using RSF from the constructor.

In Situ Quartz Crystal Microbalance (QCM) Measurements

In situ QCM measurements were acquired with a Colnatec Eon-LT monitor system, using an HT quartz crystal covered by an aluminum alloy (6 MHz initial oscillation frequency) located on the cover lid of the reactor. The signal was recorded every 0.1 s, the lowest thickness step precision was 0.04 Å, and the signal averaged over 10 cycles. The conversion of the signal to mass variation was made using impedance acoustic value of Zf = 1.00 and density of 5.88 g cm^{-3} for GaO_x, and 3.365 g cm^{-3} for GaS_x, as input parameters. Measurements were done after a stabilization time of 1 h to reach a uniform and constant temperature in the whole reaction chamber (ΔT ± 1.5 °C) and on 15 nm-Al_2O_3. Longer pulse and purge times were chosen to account for the larger reactor volume in QCM configuration and ensure an effective saturation state.

Density Functional Theory (DFT) calculations

The reactivity between gallium precursors and SiO_2 substrate was studied with gas-phase reactions with $Si(OH)_4$ (g) representing the substrate. The reaction energies were computed with the Density Functional Theory (DFT) software package CP2K with exclusion of entropy, zero-point energy and PV where P represents the pressure and V the volume. [107] Consequently, the reaction energies shed light on precursor reactivity and coordination chemistry, but they do not address the full surface chemistry. All DFT simulations were done with the Generalised Gradient Approximation (GGA) exchange-correlation functional established by Perdew, Burke and Ernzerhof, with molecularly optimised Double-Zeta Valence Polarised (DZVP) Gaussian basis functions, and with pseudopotentials established by Goedecker, Teter and Hutter.[108–110] At the start of each DFT calculation, each molecule was placed in a periodic box with 10 Angstrom of vacuum applied to each side to avoid interaction between molecules from different boxes. For each simulation, the plane-wave cutoff of the finest grid in real space fell in the range from 400 Ry to 900 Ry, and the cutoff that controlled the mapping of Gaussian's on the real-space grids fell in the range from 30 Ry to 60 Ry. A Broyden–Fletcher–Goldfarb–Shanno (BFGS) algorithm was used to optimise atomic positions such that the maximum and root-mean-square (RMS) atomic force were less than $1{\cdot}10^{-4}$ Ha/Bohr, and such that the maximum and RMS change in molecular configuration between two optimization steps were less than $1{\cdot}10^{-2}$ Bohr and $5{\cdot}10^{-3}$ Bohr, respectively. After each relaxation of atomic coordinates, the molecular frequencies were computed. In case of at least one imaginary frequency, the coordinates corresponding to the largest imaginary frequency were used to modify the relaxed molecular structure, and the atomic positions of this modified structure were optimised again. This procedure was repeated until all imaginary modes

View Article Online
DOI: 10.1039/D4DT03498H

had vanished, thus ensuring that we found the proper molecular configuration. All final optimised atomic positions are listed in the Supplementary Information.

Author contributions

E. P.: formal analysis, data curation, and writing of the original draft. D. C.: formal analysis, data curation, and investigation. P.-A. P.: formal analysis, data curation, and investigation. J. H.: formal analysis and investigation. B. v.d.L.: formal analysis, data curation. N. C.: formal analysis, data curation. S. B.: formal analysis, data curation. G. P.: formal analysis, data curation. M. B.: formal analysis, data curation, and investigation. A. A.: formal analysis, funding acquisition, writing of the original draft. N. S.: lead formal analysis, data curation, funding acquisition, writing of the original draft. All authors discussed the results and contributed to the final manuscript.

Conflicts of interest

There are no conflicts to declare.

Data availability

The data supporting this article have been included as part of the Supplementary Information. Crystallographic data for **LLi** and **$LGaCl_2$** has been deposited at the CCDC under 2409944 and 2409945.

Acknowledgements

This work was supported by the French Agence Nationale de la Recherche under the contract number HANAMI ANR-17-CE09-0022. This work has been partly carried out at the Energy4Climate Interdisciplinary Center (E4C) of IP Paris and Ecole des Ponts ParisTech, which is in part supported by 3rd Programme d'Investissements d'Avenir [ANR-18-EUR-0006-02], and by the Foundation of Ecole polytechnique (Chaire "Défis Technologiques pour une Énergie Responsable" financed by TotalEnergies) for E.P. The authors also want to thank FWO for providing the Strategic Basic Research Fellowship under the project number 1SH9E24N for B. v. d. L. The authors thank CNRS and Ecole polytechnique for financial support.

References

1 K. M. Engle and J.-Q. Yu, *J. Org. Chem.*, 2013, **78**, 8927–8955.
2 C. Chen, S. M. Bellows and P. L. Holland, *Dalton Trans.*, 2015, **44**, 16654–16670.
3 R. O. Pankov, D. O. Prima and V. P. Ananikov, *Coord. Chem. Rev.*, 2024, **516**, 215897.
4 M. L. Clarke and J. J. R. Frew, in *Organometallic Chemistry*, eds. I. J. S. Fairlamb and J. M. Lynam, Royal Society of Chemistry, Cambridge, 2009, vol. 35, pp. 19–46.
5 R. M. Bullock, *Chem. - Eur. J.*, 2004, **10**, 2366–2374.
6 S. E. Clapham, A. Hadzovic and R. H. Morris, *Coord. Chem. Rev.*, 2004, **248**, 2201–2237.
7 N. T. S. Phan, M. Van Der Sluys and C. W. Jones, *Adv. Synth. Catal.*, 2006, **348**, 609–679.
8 S. J. Firsan, V. Sivakumar and T. J. Colacot, *Chem. Rev.*, 2022, **122**, 16983–17027.
9 R. A. Collins, A. F. Russell and P. Mountford, *Appl. Petrochem. Res.*, 2015, **5**, 153–171.
10 C. Bariashir, C. Huang, G. A. Solan and W.-H. Sun, *Coord. Chem. Rev.*, 2019, **385**, 208–229.
11 T. W. Lyons and M. S. Sanford, *Chem. Rev.*, 2010, **110**, 1147–1169.
12 G. Hilt, *ChemCatChem*, 2014, **6**, 2484–2485.
13 A. Nakamura, S. Ito and K. Nozaki, *Chem. Rev.*, 2009, **109**, 5215–5244.
14 E. Fazekas, P. A. Lowy, M. Abdul Rahman, A. Lykkeberg, Y. Zhou, R. Chambenahalli and J. A. Garden, *Chem. Soc. Rev.*, 2022, **51**, 8793–8814.
15 I. Nifant'ev and P. Ivchenko, *Molecules*, 2019, **24**, 4117.
16 A. Pfaltz and W. J. Drury, *Proc. Natl. Acad. Sci. U.S.A.*, 2004, **101**, 5723–5726.
17 M. J. Burk, *Acc. Chem. Res.*, 2000, **33**, 363–372.
18 P. J. Guiry and C. P. Saunders, *Adv. Synth. Catal.*, 2004, **346**, 497–537.
19 F. Fache, E. Schulz, M. L. Tommasino and M. Lemaire, *Chem. Rev.*, 2000, **100**, 2159–2232.
20 C. Copéret, A. Comas-Vives, M. P. Conley, D. P. Estes, A. Fedorov, V. Mougel, H. Nagae, F. Núñez-Zarur and P. A. Zhizhko, *Chem. Rev.*, 2016, **116**, 323–421.
21 S. M. J. Beer, A. Krusenbaum, M. Winter, C. Vahlas and A. Devi, *Eur. J. Inorg. Chem.*, 2020, **2020**, 3587–3596.
22 A. R. Mouat, A. U. Mane, J. W. Elam, M. Delferro, T. J. Marks and P. C. Stair, *Chem. Mater.*, 2016, **28**, 1907–1919.
23 A. R. Choi, S. Seo, S. Kim, D. Kim, S.-W. Ryu, W.-J. Lee and I.-K. Oh, *Appl. Surf. Sci.*, 2023, **624**, 157104.
24 S. T. Barry, *Coord. Chem. Rev.*, 2013, **257**, 3192–3201.
25 A. Devi, *Coord. Chem. Rev.*, 2013, **257**, 3332–3384.
26 S. B. Kim, C. Yang, T. Powers, L. M. Davis, X. Lou and R. G. Gordon, *Angew Chem Int Ed*, 2016, **55**, 10228–10233.
27 Q. Fan, L. Sang, D. Jiang, L. Yang, H. Zhang, Q. Chen and Z. Liu, *J. Vac. Sci. Technol. A: Vac. Surf. Films*, 2019, **37**, 010904.
28 X. Wang, *ECS Transactions*, 2017, **80**, 77.
29 R. Zhao, Z. Guo and X. Wang, *J. Phys. Chem. C*, 2018, **122**, 21514–21520.
30 B. Lee, K. J. Choi, A. Hande, M. J. Kim, R. M. Wallace, J. Kim, Y. Senzaki, D. Shenai, H. Li, M. Rousseau and J. Suydam, *Microelectron. Eng.*, 2009, **86**, 272–276.
31 Z. Li, A. Rahtu and R. G. Gordon, *J. Electrochem. Soc.*, 2006, **153**, C787.
32 S. B. Kim, X. Zhao, L. M. Davis, A. Jayaraman, C. Yang and R. G. Gordon, *ACS Appl. Mater. Interfaces*, 2019, **11**, 45892–45902.
33 S. Chen, J. Ren, D. Yang, L. Sang, B. Liu, Q. Chen and Z. Liu, *J. Vac. Sci. Technol. A*, 2023, **41**, 042401.
34 T. E. Shaw, Z. Ali, T. M. Currie, S. N. Berriel, B. Butkus, J. T. Wagner, K. Preradovic, G. P. A. Yap, J. C. Green, P. Banerjee, A. P. Sattelberger, L. McElwee-White and T. Jurca, *ACS Appl. Mater. Interfaces*, 2023, **15**, 35590–35599.
35 Z. Guo, H. Li, Q. Chen, L. Sang, L. Yang, Z. Liu and X. Wang, *Chem. Mater.*, 2015, **27**, 5988–5996.
36 S. Seppälä, J. Niinistö, M. Mattinen, K. Mizohata, J. Räisänen, W. Noh, M. Ritala and M. Leskelä, *Thin Solid Films*, 2018, **660**, 199–206.

37 S. Seppälä, J. Niinistö, T. Blanquart, M. Kaipio, K. Mizohata, J. Räisänen, C. Lansalot-Matras, W. Noh, M. Ritala and M. Leskelä, *Chem. Mater.*, 2016, **28**, 5440–5449.
38 M. Golalikhani, T. James, P. Van Buskirk, W. Noh, J. Lee, Z. Wang and J. F. Roeder, *J. Vac. Sci. Technol. A: Vac. Surf. Films*, 2018, **36**, 051502.
39 T. Blanquart, M. Kaipio, J. Niinistö, M. Gavagnin, V. Longo, L. Blanquart, C. Lansalot, W. Noh, H. D. Wanzenböck, M. Ritala and M. Leskelä, *Chem. Vap. Depos.*, 2014, **20**, 217–223.
40 H. Yoon, Y. Lee, G. Y. Lee, S. Seo, B. K. Park, T.-M. Chung, I.-K. Oh and H. Kim, *J. Chem. Phys.*, 2024, **160**, 024302.
41 P. J. Pallister, S. C. Buttera and S. T. Barry, *J. Phys. Chem. C*, 2014, **118**, 1618–1627.
42 O. Maimon and Q. Li, *Materials*, 2023, **16**, 7693.
43 S. Sun, C. Wang, S. Alghamdi, H. Zhou, Y. Hao and J. Zhang, *Adv. Elect. Materials*, 2024, 2300844.
44 Y. Qin, Z. Wang, K. Sasaki, J. Ye and Y. Zhang, *Jpn. J. Appl. Phys.*, 2023, **62**, SF0801.
45 Y. Zheng, X. Tang, W. Wang, L. Jin and G. Li, *Adv. Funct. Materials*, 2021, **31**, 2008307.
46 L. Hu and D. Wei, *J. Phys. Chem. C*, 2018, **122**, 27795–27802.
47 M. M. Y. A. Alsaif, N. Pillai, S. Kuriakose, S. Walia, A. Jannat, K. Xu, T. Alkathiri, M. Mohiuddin, T. Daeneke, K. Kalantar-Zadeh, J. Z. Ou and A. Zavabeti, *ACS Appl. Nano Mater.*, 2019, **2**, 4665–4672.
48 I. Donmez, C. Ozgit-Akgun and N. Biyikli, *J. Vac. Sci. Technol. A: Vac. Surf. Films*, 2013, **31**, 01A110.
49 C. Ozgit, I. Donmez, M. Alevli and N. Biyikli, *J. Vac. Sci. Technol. A: Vac. Surf. Films*, 2012, **30**, 01A124.
50 N. Biyikli, C. Ozgit and I. Donmez, *Nanosci. Nanotechnol. Lett.*, 2012, **4**, 1008–1014.
51 C. Ozgit-Akgun, E. Goldenberg, A. K. Okyay and N. Biyikli, *J. Mater. Chem. C*, 2014, **2**, 2123–2136.
52 S. Bolat, C. Ozgit-Akgun, B. Tekcan, N. Biyikli and A. K. Okyay, *Appl. Phys. Lett.*, 2014, **104**, 243505.
53 B. T. McDermott, K. G. Reid, N. A. El-Masry, S. M. Bedair, W. M. Duncan, X. Yin and F. H. Pollak, *Appl. Phys. Lett.*, 1990, **56**, 1172–1174.
54 E. Graugnard, V. Chawla, D. Lorang and C. J. Summers, *Appl. Phys. Lett.*, 2006, **89**, 211102.
55 J. Kuhs, Z. Hens and C. Detavernier, *J. Vac. Sci. Technol. A: Vac. Surf. Films*, 2019, **37**, 020915.
56 A. V. Uvarov, A. S. Gudovskikh, V. N. Nevedomskiy, A. I. Baranov, D. A. Kudryashov, I. A. Morozov and J.-P. Kleider, *J. Phys. D: Appl. Phys.*, 2020, **53**, 345105.
57 T. G. Allen and A. Cuevas, *Phys. Status Solidi - Rapid Res. Lett.*, 2015, **9**, 220–224.
58 H.-P. Ma, X.-X. Li, J.-H. Yang, P. Cheng, W. Huang, J. Zhu, T.-C. Jen, Q. Guo, H.-L. Lu and D. W. Zhang, *Chem. Mater.*, 2019, **31**, 7405–7416.
59 D. J. Comstock and J. W. Elam, *Chem. Mater.*, 2012, **24**, 4011–4018.
60 T. G. Allen and A. Cuevas, *Appl. Phys. Lett.*, 2014, **105**, 031601.
61 D. Hiller, J. Julin, A. Chnani and S. Strehle, *IEEE J. Photovoltaics*, 2020, **10**, 959–968.
62 V. D. Wheeler, N. Nepal, D. R. Boris, S. B. Qadri, L. O. Nyakiti, A. Lang, A. Koehler, G. Foster, S. G. Walton, C. R. Eddy and D. J. Meyer, *Chem. Mater.*, 2020, **32**, 1140–1152.
63 H.-Y. Shih, F.-C. Chu, A. Das, C.-Y. Lee, M.-J. Chen and R.-M. Lin, *Nanoscale Res. Lett.*, 2016, **11**, 235.
64 J. W. Roberts, P. R. Chalker, B. Ding, R. A. Oliver, J. T. Gibbon, L. A. H. Jones, V. R. Dhanak, L. J. Phillips, J. D. Major and F. C.-P. Massabuau, *J. Cryst. Growth.*, 2019, **528**, 125254.
65 E. Rafie Borujeny, O. Sendetskyi, M. D. Fleischauer and K. C. Cadien, *ACS Appl. Mater. Interfaces*, 2020, **12**, 44225–44237.
66 S. Ilhom, A. Mohammad, D. Shukla, J. Grasso, B. G. Willis, A. K. Okyay and N. Biyikli, *ACS Appl. Mater. Interfaces*, 2021, **13**, 8538–8551.
67 S. Wang, Y. Zhao, N. Cheng, Y. Ren, X. Liu, L. Li, Y. Jia, Y. Guan, H. Chen and S. Peng, *Mater. Chem. Phys.*, 2023, **306**, 128037.
68 M. Asif Khan, R. A. Skogman, J. M. Van Hove, D. T. Olson and J. N. Kuznia, *Appl. Phys. Lett.*, 1992, **60**, 1366–1368.
69 J. Sumakeris, Z. Sitar, K. S. Ailey-Trent, K. L. More and R. F. Davis, *Thin Solid Films*, 1993, **225**, 244–249.
70 M. Asif Khan, J. N. Kuznia, D. T. Olson, T. George and W. T. Pike, *Appl. Phys. Lett.*, 1993, **63**, 3470–3472.
71 S. Choi, A. S. Ansari, H. J. Yun, H. Kim, B. Shong and B. J. Choi, *J. Alloys Compd.*, 2021, **854**, 157186.
72 H.-Y. Shih, M.-C. Lin, L.-Y. Chen and M.-J. Chen, *Nanotechnol.*, 2015, **26**, 014002.
73 P. Deminskyi, C.-W. Hsu, B. Bakhit, P. Rouf and H. Pedersen, *J. Vac. Sci. Technol. A*, 2021, **39**, 012411.
74 A. Haider, S. Kizir, C. Ozgit-Akgun, E. Goldenberg, S. A. Leghari, A. K. Okyay and N. Biyikli, *J. Mater. Chem. C*, 2015, **3**, 9620–9630.
75 P. Motamedi, N. Dalili and K. Cadien, *J. Mater. Chem. C*, 2015, **3**, 7428–7436.
76 P. Motamedi and K. Cadien, *RSC Adv.*, 2015, **5**, 57865–57874.
77 M. Alevli, N. Gungor, A. Haider, S. Kizir, S. A. Leghari and N. Biyikli, *J. Vac. Sci. Technol. A: Vac. Surf. Films*, 2016, **34**, 01A125.
78 S. Kizir, A. Haider and N. Biyikli, *J. Vac. Sci. Technol. A: Vac. Surf. Films*, 2016, **34**, 041511.
79 M. Yoshimoto, A. Kajimoto and H. Matsunami, *Thin Solid Films*, 1993, **225**, 70–73.
80 A. K. Akinori Koukitu, Y. K. Yoshinao Kumagai, T. T. Tetsuya Taki and H. S. Hisashi Seki, *Jpn. J. Appl. Phys.*, 1999, **38**, 4980.
81 Y. Kumagai, M. Mayumi, A. Koukitu and H. Seki, *Appl. Surf. Sci.*, 2000, **159–160**, 427–431.
82 H. Tsuchiya, M. Akamatsu, M. I. Masahiko Ishida and F. H. Fumio Hasegawa, *Jpn. J. Appl. Phys.*, 1996, **35**, L748.
83 O. H. Kim, D. Kim and T. Anderson, *J. Vac. Sci. Technol. A: Vac. Surf. Films*, 2009, **27**, 923–928.
84 X. Meng, J. A. Libera, T. T. Fister, H. Zhou, J. K. Hedlund, P. Fenter and J. W. Elam, *Chem. Mater.*, 2014, **26**, 1029–1039.
85 X. Meng, K. He, D. Su, X. Zhang, C. Sun, Y. Ren, H. Wang, W. Weng, L. Trahey, C. P. Canlas and J. W. Elam, *Adv. Funct. Materials*, 2014, **24**, 5435–5442.
86 N. Schneider, M. Frégnaux, M. Bouttemy, F. Donsanti, A. Etcheberry and D. Lincot, *Mater. Today Chem.*, 2018, **10**, 142–152.
87 F. Mathew, N. Poonkottil, E. Solano, D. Poelman, Z. Hens, C. Detavernier and J. Dendooven, *J. Vac. Sci. Technol. A: Vac. Surf. Films*, 2023, **41**, 060401.
88 P. Rouf, N. J. O'Brien, S. C. Buttera, I. Martinovic, B. Bakhit, E. Martinsson, J. Palisaitis, C.-W. Hsu and H. Pedersen, *J. Mater. Chem. C*, 2020, **8**, 8457–8465.
89 R. O'Donoghue, J. Rechmann, M. Aghaee, D. Rogalla, H.-W. Becker, M. Creatore, A. D. Wieck and A. Devi, *Dalton Trans.*, 2017, **46**, 16551–16561.
90 Dezelah, J. Niinistö, K. Arstila, L. Niinistö and C. H. Winter, *Chem. Mater.*, 2006, **18**, 471–475.

View Article Online
DOI: 10.1039/D4DT03498H

91 M. Nieminen, L. Niinistö and E. Rauhala, *J. Mater. Chem.*, 1996, **6**, 27–31.
92 S. Dagorne, R. F. Jordan and V. G. Young, *Organometallics*, 1999, **18**, 4619–4623.
93 J. L. Bourque, M. C. Biesinger and K. M. Baines, *Dalton Trans.*, 2016, **45**, 7678–7696.
94 J. F. Moulder, W. F. Stickle, P. E. Sobol and K. D. Bomben, *Handbook of X-ray Photelectron Spectroscopy: a Reference Book of Standard Spectra for Identification and Interpretation of XPS Data*, Physical Electronics, Eden Prairie, Minn., 1995.
95 S. C. Ghosh, M. C. Biesinger, R. R. LaPierre and P. Kruse, *J. Appl. Phys.*, 2007, **101**, 114322.
96 K. Doo-Hyun, Y. Seung-Ho, C. Taek-Mo, A. Ki-Seok, Y. Hee-Soo and K. Yunsoo, *Bull. Korean Chem. Soc.*, 2002, **23**, 225–228.
97 D. L. Reger, S. J. Knox and L. Lebioda, *Organometallics*, 1990, **9**, 2218–2222.
98 D. Solis-Ibarra, A. P. Gómora-Figueroa, N. Zavala-Segovia and V. Jancik, *Eur. J. Inorg. Chem.*, 2009, **2009**, 4564–4571.
99 Z. Xiao, G. Passeri, J. Northcote-Smith, K. Singh and K. Suntharalingam, *Chem. - Eur. J.*, 2021, **27**, 13846–13854.
100 T. Řičica, Y. Milasheuskaya, Z. Růžičková, P. Němec, P. Švanda, Z. O. Zmrhalová, R. Jambor and M. Bouška, *Chem. Asian J.*, 2019, **14**, 4229–4235.
101 Z. Hu and C. H. Turner, *J. Phys. Chem. B*, 2006, **110**, 8337–8347.
102 S. Grimme, J. Antony, S. Ehrlich and H. Krieg, *The Journal of Chemical Physics*, 2010, **132**, 154104.
103 A. Mahmoodinezhad, C. Janowitz, F. Naumann, P. Plate, H. Gargouri, K. Henkel, D. Schmeißer and J. I. Flege, *J. Vac. Sci. Technol. A: Vac. Surf. Films*, 2020, **38**, 022404.
104 C.-Y. Shi, Q.-Z. Chen, Z.-X. Zhang, C.-H. Hsu, M.-J. Zhao, X.-Y. Zhang, P. Gao, W.-Y. Wu, D.-S. Wuu, C.-J. Huang, S.-Y. Lien and W.-Z. Zhu, *J. Mater. Chem. C*, 2022, **10**, 17974–17982.
105 A. S. Ansari, S. S. Raya and B. Shong, *J. Phys. Chem. C*, 2020, **124**, 17121–17134.
106 H. Fujiwara, *Spectroscopic Ellipsometry for Photovoltaics: Volume 2: Applications and Optical Data of Solar Cell Materials*, Springer International Publishing AG, Cham, 2019.
107 T. D. Kühne, M. Iannuzzi, M. Del Ben, V. V. Rybkin, P. Seewald, F. Stein, T. Laino, R. Z. Khaliullin, O. Schütt, F. Schiffmann, D. Golze, J. Wilhelm, S. Chulkov, M. H. Bani-Hashemian, V. Weber, U. Borštnik, M. Taillefumier, A. S. Jakobovits, A. Lazzaro, H. Pabst, T. Müller, R. Schade, M. Guidon, S. Andermatt, N. Holmberg, G. K. Schenter, A. Hehn, A. Bussy, F. Belleflamme, G. Tabacchi, A. Glöß, M. Lass, I. Bethune, C. J. Mundy, C. Plessl, M. Watkins, J. VandeVondele, M. Krack and J. Hutter, *J. Chem. Phys.*, 2020, **152**, 194103.
108 J. P. Perdew, K. Burke and M. Ernzerhof, *Phys. Rev. Lett.*, 1996, **77**, 3865–3868.
109 J. VandeVondele and J. Hutter, *The Journal of Chemical Physics*, 2007, **127**, 114105.
110 S. Goedecker, M. Teter and J. Hutter, *Phys. Rev. B*, 1996, **54**, 1703–1710.

View Article Online
DOI: 10.1039/D4DT03498H

ARTICLE

Unveiling surface reactivity: the crucial role of auxiliary ligands in Gallium amidinate-based precursors for Atomic Layer Deposition

Received 00th January 20xx,
Accepted 00th January 20xx

DOI: 10.1039/x0xx00000x

Eva Pugliese,[a,b] Damien Coutancier,[a] Paul-Alexis Pavard,[a] Julien Hervochon,[a] Bram van der Linden,[c,d] Nicolas Casaretto,[b] Sophie Bourcier,[b] Geoffrey Pourtois,[d] Muriel Bouttemy,[a,e] Audrey Auffrant,[b] and Nathanaelle Schneider[a,*]

Data Availability Statement (DAS)

The data supporting this article have been included as part of the Supplementary Information. Crystallographic data for **LLi** and **$LGaCl_2$** has been deposited at the CCDC under 2409944 and 2409945.

[a.] *Institut Photovoltaïque d'Île-de-France (IPVF), UMR 9006, CNRS, Ecole Polytechnique - IP Paris, Chimie Paristech - PSL, 18 Boulevard Thomas Gobert, Palaiseau, 91120, France*
[b.] *Laboratoire de Chimie Moléculaire (LCM), CNRS, École Polytechnique, Institut Polytechnique de Paris, Route de Saclay, 91120 Palaiseau, France.*
[c.] *Department of Chemistry, KU Leuven, Celestijnenlaan 200F, 3001 Leuven, Belgium*
[d.] *IMEC, Kapeldreef 75, 3001 Leuven, Belgium*
[e.] *Institut Lavoisier de Versailles (ILV), Université de Versailles Saint-Quentin-en-Yvelines, Université Paris-Saclay, CNRS, UMR 8180, 78035Versailles CEDEX, France*
† Email: nathanaelle.schneider@cnrs.fr.
Supplementary Information available: See DOI: 10.1039/x0xx00000x